JOURNAL OF THERMOPHYSICS AND HEAT TRANSFER
Vol. 25, No. 1, January–March 2011

# Effect of Chemical Reaction Rates on Aeroheating Predictions of Reentry Flows

D. Siva K. Reddy* and Krishnendu Sinha†
*Indian Institute of Technology Bombay, Mumbai 400 076, India*

DOI: 10.2514/1.47635

**The present work deals with the sensitivity of aeroheating predictions to variations in chemical reaction rates in high-enthalpy flows over reentry capsules. Within this scope, numerical simulations are performed by varying the reaction rate constants over their uncertainty range. FIRE 2 reentry capsule at 35 km altitude is chosen as the test case. At these conditions, recombination of oxygen atoms is the dominant chemical reaction in the thermal boundary layer near the wall. The flow solutions computed by altering the reaction rates are carefully analyzed to understand the physical effects that influence the surface heat transfer rate. It is found that the chemical state of the gas, i.e., equilibrium, nonequilibrium or frozen, and the extent of recombination reactions in the boundary layer are the critical factors that determine the sensitivity of the heating rate to variations in the reaction rate constants. The analysis is carried out at different points on the vehicle surface, and the heating rate sensitivity is found to be highest at the shoulder. This is due to the nonequilibrium chemical state of the gas prevailing in the shoulder expansion region. By comparison, the equilibrium state of the gas on the forebody and the frozen chemistry on the afterbody result in lower sensitivity of the heating rate to variations in the chemical reaction rates.**

## Nomenclature

| | | |
|---|---|---|
| $C_f$ and $\eta$ | = | coefficients for the calculation of a chemical reaction rate |
| $D$ | = | diameter of the vehicle, m |
| $K_{\text{eq}}$ | = | equilibrium constant |
| $k_b$ | = | backward reaction rate coefficient, $m^3/(kg\text{-}mol.s)$ or $m^6/(kg\text{-}mol^2.s)$ |
| $k_f$ | = | forward reaction rate coefficient, $m^3/(kg\text{-}mol.s)$ |
| $l$ | = | wall-normal distance, m |
| $M$ | = | molecular weight |
| $p$ | = | pressure, Pa |
| $q$ | = | heat transfer rate, $W/cm^2$ |
| $R$ | = | net reaction rate for a chemical reaction, $kg\text{-}mol/(m^3.s)$ |
| $s$ | = | arc length measured from nose stagnation point, m |
| $T$ | = | translational-rotational temperature, K |
| $T_a$ | = | geometrically-averaged temperature, K |
| $T_v$ | = | vibrational temperature, K |
| $Y$ | = | species mass fraction |
| $\delta$ | = | thermal boundary-layer thickness, m |
| $\theta_d$ | = | characteristic temperature for a chemical reaction |
| $\kappa$ | = | thermal conductivity, W/m.K |
| $\mu$ | = | molecular viscosity, Pa · s |
| $\nu_T$ | = | turbulent kinematic viscosity, $m^2/s$ |

*Subscripts*

| | | |
|---|---|---|
| $i$ | = | species number |
| $n$ | = | reaction number |
| $w$ | = | wall |
| 2 | = | cell next to the wall in the computational grid |

Presented as Paper 2010-0630 at the 48th AIAA Aerospace Sciences Meeting, Orlando, FL, 4–7 January 2010; received 21 December 2009; revision received 16 July 2010; accepted for publication 24 September 2010. 

*Doctoral Student, Department of Aerospace Engineering.
†Assistant Professor, Department of Aerospace Engineering. Member AIAA.

## I. Introduction

REENTRY flowfields are characterized by high-temperature effects, such as excitation of internal energy modes, chemical reactions, and ionization. Accuracy of the computational predictions of such flowfields and the associated aerothermal loads depends on accurate modeling of these high-temperature effects. The physical models for the high-temperature phenomena are developed based on experimentally obtained thermal relaxation rates and chemical reaction rate constants. These parameters, commonly referred to as kinetic data, are essential for the closure of the energy exchange rate equations that are used in computational fluid dynamics (CFD) simulation of high-enthalpy flows.

The flowfield solution obtained using CFD methods is sensitive to the kinetic data being used. STS-1 flight data [1] and computational studies of the X-33 vehicle [2] indicate that aerodynamics of control surfaces are affected by high-temperature effects, which in turn depend on kinetic data. Investigation of high-enthalpy flows over double-cone configurations by Candler and Olejniczak [3] reveal that the computed size of separation bubble at the cone-cone junction is sensitive to the chemical reaction rate models used in the CFD formulation. In a review of aerothermal effects in reentry flowfields, Gnoffo et al. [4] recommend isolated parametric studies of physical modeling parameters including reaction rate constants. These studies can provide insight into the dominant mechanisms that are affecting the heating rate.

Bose and Wright [5] use Monte Carlo sensitivity and uncertainty analysis to study the effect of thermochemical modeling parameters on stagnation point heat transfer rate. The freestream conditions correspond to the peak heating condition of the Mars pathfinder vehicle. They vary several parameters, including reaction rate constants, diffusion coefficients and surface catalysis parameters, and perform a large number of simulations to quantify their effect on the heating rate. They study different flow regimes based on the wall catalytic behavior, and identify the dominant parameters affecting the heating rate. For supercatalytic surfaces, the stagnation point heat transfer rate is primarily sensitive to the diffusion parameter, whereas oxygen atom recombination rate is found to be the dominant parameter in the weakly catalytic regime. Similar uncertainty analysis is performed by Palmer [6] for crew exploration vehicle at conditions representative of low earth orbit and lunar return entries. The study includes radiative effects in addition to convective heating and finds that changes in radiative heating is less than those in the convective heating due to variation in key input parameters.

Tchuen and Zeitoun [7] study the effect of chemistry in high-enthalpy nonequilibrium flows around blunt bodies. The chosen test

cases span a range of the freestream Mach number, density and stagnation enthalpy. They compute the flowfields and surface properties with different reaction rates available in literature, and compare the results with available experimental data. The shock standoff distance and peak translational temperature at the shock wave are found to be sensitive to the reaction rates used in the simulations. Differences are also observed in the species mass fraction in the shock layer and boundary layer, leading to variation in the computed surface properties. The stagnation point heating rates computed using various reaction rates are found to differ by up to 60%.

In the preceding studies, heating rate predictions change significantly due to variations in thermochemical parameters used in the simulations. The surface heat flux variations depend largely on the freestream conditions. Even at a single freestream condition, the heating rate is sensitive to different parameters depending on the surface conditions. In light of these findings, it is important to understand how the changes in the chemical reaction rates influence the gas properties and the surface heating. A study of the underlying physical mechanisms is required so that we can identify the critical factors that determine the sensitivity of the heating rate to the variations in kinetic data. The current work is a step in this direction.

The test case chosen in this work corresponds to the FIRE 2 reentry capsule at 35 km altitude trajectory point (1652.75 s after launch). The freestream density and temperature are 0.0083 kg/m$^3$ and 237 K, respectively. The freestream velocity is 4950 m/s and corresponding Mach number is 16. The stagnation enthalpy is 12.5 MJ/kg, and angle of attack is assumed to be 0. The outer mold line of the capsule used in the current simulations is shown in Fig. 1, and the freestream conditions [8] are listed in Table 1. Detailed description of the computed flowfield solution and a comparison of the afterbody heat transfer rate with in-flight measurement are presented in [9].

Experimental data presented in [10] show that the uncertainty in the measurement of rate constant values may be as high as an order of magnitude. The kinetic parameters are varied accordingly from their baseline values to study their effect on heat transfer rate. The flowfield solutions obtained by using different rate constants are compared in detail to ascertain the physical effects that alter the heating rate predictions. The analysis is performed at different points on the forebody, afterbody and shoulder of the vehicle. Earlier efforts [5–7], primarily focus on the forebody heating rate. Flow expansion at the shoulder and separation on the afterbody bring in additional effects that influence the sensitivity of heating rate to the chemical kinetic parameters.

## II. Simulation Methodology

The simulation methodology used in the present work is the same as that used in [9], and a brief summary is given next. The chemically

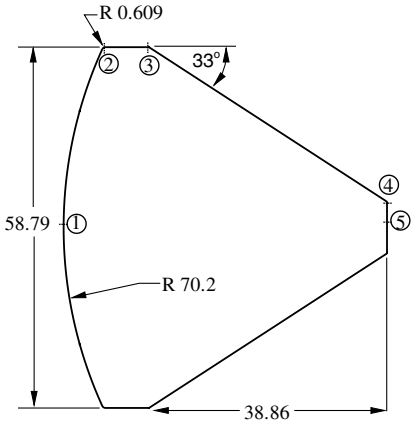


**Fig. 1 Geometry of the FIRE 2 vehicle used in the CFD simulations. All dimensions are in cm. Critical geometrical points are 1) fore stagnation point, $s/D = 0$, 2) fore shoulder, $s/D = 0.51$, 3) heatshield-backshell interface, $s/D = 0.64$, 4) aft shoulder, $s/D = 1.42$, and 5) aft stagnation point, $s/D = 1.5$.**

**Table 1 Freestream conditions for the simulations**

| Freestream conditions | |
|---|---|
| Time from launch, sec | 1652.75 |
| Altitude, km | 35 |
| $\rho_\infty$, kg/m$^3$ | 0.0083 |
| $U_\infty$, m/s | 4950 |
| $T_\infty$, K | 237 |
| $M_\infty$ | 16 |
| $T_w$, K | 553.3 |
| Angle of attack, deg | 0 |
| $H_0$, MJ/kg | 12.5 |

reacting turbulent hypersonic flow around the reentry configuration is simulated by solving the Reynolds-averaged Navier–Stokes equations along with the species conservation equations and a thermal nonequilibrium model. Air is modeled as a neutral mixture of five perfect species ($N_2$, $O_2$, NO, N and O) with three dissociation and two exchange reactions. The two-temperature model of Park [10] is used to describe the thermal state of the gas. An additional conservation equation is solved for the vibrational energy of the mixture to account for the thermal nonequilibrium. The Arrhenius rate constants for the chemical reactions are evaluated using curve fits to experimental data by Park [10]. The molecular viscosity of each species is determined using curve fit data of Blottner et al. [11]. Thermal conductivities for the translational and rotational modes of the species are then determined using the Eucken relation [12]. Viscosity and thermal conductivity of the mixture are computed using Wilke's mixing rule [13]. Multicomponent mass diffusion due to concentration gradient is modeled using Fick's law with a Lewis number of 1.4.

The axisymmetric form of the governing equations are discretized using the finite volume approach. Inviscid fluxes are computed using a modified (low-dissipation) form of the Steger–Warming flux splitting approach [14], and the turbulence model equations are fully coupled to the mean flow equations [15]. The method is second-order accurate in both streamwise and wall-normal directions. The viscous fluxes and the turbulent source terms are evaluated using second-order accurate central differencing and the implicit data parallel line relaxation method [16] is used to obtain steady-state solutions. The Spalart–Allmaras (SA) model [17] is used for turbulence closure. No-slip, noncatalytic and isothermal boundary conditions are specified at the wall. Both $T$ and $T_v$ are set to the isothermal temperature $T_w$ at the wall. The boundary conditions for SA turbulence model are $\nu_{T\infty} = 0.1\mu_\infty/\rho_\infty$ and $\nu_{T,w} = 0$ as given in [17]. Freestream conditions are applied at the outer boundary and extrapolation boundary condition is imposed at the exit station.

Note that the original SA model without compressibility corrections is used in the current simulations. The effect of compressibility corrections is discussed in [9]. The corrections tend to reduce the turbulence levels in the recirculation bubble. This increases the surface pressure and reduces the heat transfer rate on the afterbody. Based on comparison with flight data the compressibility corrections are found to have a detrimental effect on the turbulence model predictions and therefore these corrections are not included in the current work.

The grid used in the simulations is shown in Fig. 2. The outer boundary follows the shape of the bow shock and extends up to 2.5 diameters downstream of the vehicle base. The flow at this point is found to be supersonic and therefore the location of the exit boundary is not expected to alter the flow solution in the vicinity of the vehicle. The grid consists of 240 points in the wall-parallel direction and 170 points in the wall-normal direction. The wall-normal spacing at the vehicle surface is $1 \times 10^{-6}$ m. The variation in surface heat flux due to further decrease in wall-normal spacing is less than 0.2% of the nose stagnation point value. The afterbody heating rate is sensitive to the grid quality in the recirculation bubble and free shear layer. Data presented in [9] shows that changes in afterbody heating rate due to refinement on the current grid are less than 2% of the base stagnation point value.

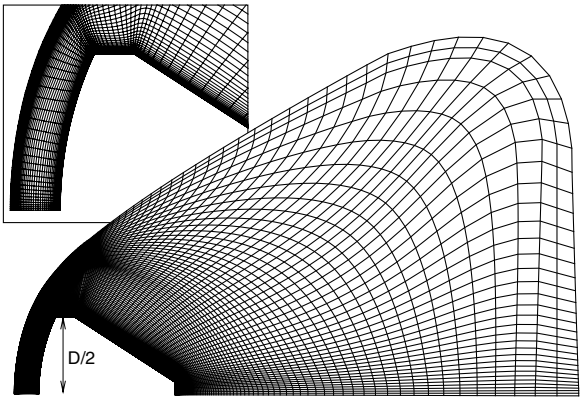


**Fig. 2 Computational grid used in the simulations. The inset shows a magnified view of the grid near the vehicle, where every second point is shown in each direction.**

The five chemical reactions considered in the present work are

$$\begin{aligned} &N_2 + M \rightleftharpoons 2N + M \qquad O_2 + M \rightleftharpoons 2O + M \\ &NO + M \rightleftharpoons N + O + M \qquad N_2 + O \rightleftharpoons NO + N \\ &NO + O \rightleftharpoons O_2 + N \end{aligned} \tag{1}$$

The first three reactions represent dissociation of molecular nitrogen, oxygen and nitric oxide. M is the collision partner, which provides the required energy to break the chemical bond. The collision partner can be any of the five species, and it remains unaltered in the reaction. The last two reactions are the Zeldovich exchange reactions which govern the concentration of NO in hypersonic flows. The reaction rates for the preceding five reactions are given by

$$\begin{aligned} R_1 &= \sum_{m=1}^{5}\left[k_{b_{1m}}\frac{\rho_N}{M_N}\frac{\rho_N}{M_N}\frac{\rho_m}{M_m} - k_{f_{1m}}\frac{\rho_{N_2}}{M_{N_2}}\frac{\rho_m}{M_m}\right] \\ R_2 &= \sum_{m=1}^{5}\left[k_{b_{2m}}\frac{\rho_O}{M_O}\frac{\rho_O}{M_O}\frac{\rho_m}{M_m} - k_{f_{2m}}\frac{\rho_{O_2}}{M_{O_2}}\frac{\rho_m}{M_m}\right] \\ R_3 &= \sum_{m=1}^{5}\left[k_{b_{3m}}\frac{\rho_N}{M_N}\frac{\rho_O}{M_O}\frac{\rho_m}{M_m} - k_{f_{3m}}\frac{\rho_{NO}}{M_{NO}}\frac{\rho_m}{M_m}\right] \\ R_4 &= k_{b_4}\frac{\rho_{NO}}{M_{NO}}\frac{\rho_N}{M_N} - k_{f_4}\frac{\rho_{N_2}}{M_{N_2}}\frac{\rho_O}{M_O} \\ R_5 &= k_{b_5}\frac{\rho_{O_2}}{M_{O_2}}\frac{\rho_N}{M_N} - k_{f_5}\frac{\rho_{NO}}{M_{NO}}\frac{\rho_O}{M_O} \end{aligned} \tag{2}$$

In the preceding equations subscript $m$ indicates collision partner. $M_i$ and $\rho_i$ represent the $i$th species molecular weight and density, respectively. The parameters $k_b$ and $k_f$ are Arrhenius rate constants for backward and forward reactions, respectively, and are given by [10]

$$k_{f_n}(T_a) = C_{fn}T_a^{\eta_n}\exp(\theta_{dn}/T_a) \qquad (n = 1, \ldots, 5) \tag{3}$$

where $C_{fn}$, $\eta_n$ and $\theta_{dn}$ are experimentally determined curve fit data for the $n$th reaction over a given temperature range. $T_a$ is the effective temperature and for dissociation reactions ($n = 1, 2, 3$) it is taken as the geometric average of the translational-rotational and vibrational temperature i.e. $T_a = \sqrt{TT_v}$. For exchange reactions $T_a = T$. The backward reaction rate constant is obtained using the principle of detailed balance:

$$k_{b_n}(T) = \frac{k_{f_n}(T)}{K_{\text{eq},n}} \tag{4}$$

where $K_{\text{eq},n}$ is the equilibrium constant given in [10].

The preceding set of equations define the chemical kinetics used in the current CFD algorithm. The data presented in [10] show that the uncertainty in the measurement of rate constants is about 1 order of magnitude. Hence simulations are performed by increasing and decreasing the chemical reaction rate constants ($k_f$ and $k_b$) by 10 times compared with the baseline values. We change the rate constants for both the forward and backward reactions so that the equilibrium constant remains the same for the given local thermodynamic conditions. Similar procedure is used in [18]. Rate constants are altered for all five reactions simultaneously.

In the CFD algorithm, the reaction rates are altered by multiplying the rate constants by a reaction scaling factor (rsf). The modified forward rate constant at each point is given by rsf $* k_{f_n}$, where $k_{f_n}$ is calculated using Eq. (3). The backward reaction rates are also multiplied by the same factor. Hence a value of rsf $= 10$ corresponds to the higher reactivity case, where reaction rate constants are increased by 10 times. On the other hand, rsf $= 0.1$ represents lower reactivity case where reaction rate constants are decreased by 10 times, and rsf $= 1$ indicates baseline simulation. Note that the chemical source terms in all the simulations are evaluated using mean flow properties, such that the effect of turbulent fluctuations on the reaction rates is neglected. The interaction of turbulence and chemistry can lead to additional variation in the reaction rates, which is beyond the scope of the present paper.

The surface heat transfer rate is directly influenced by the gas composition and temperature in the thermal boundary layer adjacent to the wall. The gas properties in this region are primarily determined by the exothermic recombination reactions caused by the isothermal cold wall condition. The thermochemical reactions at the shock wave and in the inviscid postshock region affects the flow properties at the boundary-layer edge. The thermochemistry at the shock wave is predominantly endothermic and variation in the corresponding reaction rates can alter the boundary-layer edge conditions and therefore the heating rate predictions.

We first study the sensitivity of surface heat flux to the variations in reaction rates only in the boundary layer. In the baseline simulation, the maximum boundary-layer thickness is found to be 2.6 mm, which corresponds to about 80 wall-normal points in the computational grid. In this region, the reaction rates are altered by setting rsf $\neq 1$. Outside the boundary layer, a value of rsf $= 1$ is used, such that the reaction rates match the baseline values. This results in boundary-layer edge conditions that are identical to the baseline solution. Variation in fluid properties at the boundary-layer edge caused by the thermochemistry at the shock wave are subsequently studied by altering the reaction rates uniformly over the entire computational domain. A controlled study of this nature allows us to isolate the physical effects in different parts of the flowfield.

## III. Results

A brief description of the computed FIRE 2 reentry flowfield and surface properties are given next. The details of the thermochemical state of the gas and chemical reactions in the boundary layer are presented. The effect of variation in the chemical reaction rates on heating predictions is explained subsequently.

Main features of the flowfield are shown in Fig. 3 in terms of the Mach number contours. The prominent features like bow shock and flow expansion at the corners can be easily identified. The flow on the entire forebody is subsonic with Mach number approaching unity close to the first expansion corner. The postshock temperature in the nose stagnation region is about 5700 K and it varies less than 5% on the forebody. Flow expansion at the first corner results in decrease of temperature to 4100 K. Further expansion around the second corner decreases the temperature to about 1800 K.

The boundary layer remains attached through the two successive expansions, and separates downstream of the second corner. The recirculation bubble on the afterbody is characterized by a single toroidal vortex that extends up to about 0.36 diameter downstream of the base. Flow in the separation bubble is subsonic with vortex core temperature of about 4000 K. The shear layer enclosing the recirculation region coalesce at the neck, and a recompression shock wave is formed. The temperature of the gas in the neck region is close to 4900 K. The temperature in the inviscid region outside the wake is about 2000 K and the Mach number there is about 3.5.

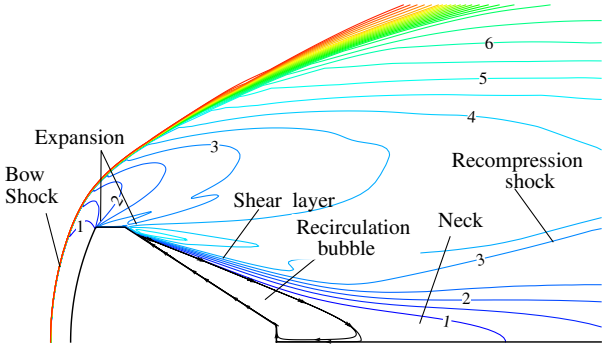


**Fig. 3 Mach number distribution in the flow around FIRE 2 reentry capsule at Mach 16. Representative streamlines are shown on the afterbody to identify the recirculation bubble.**

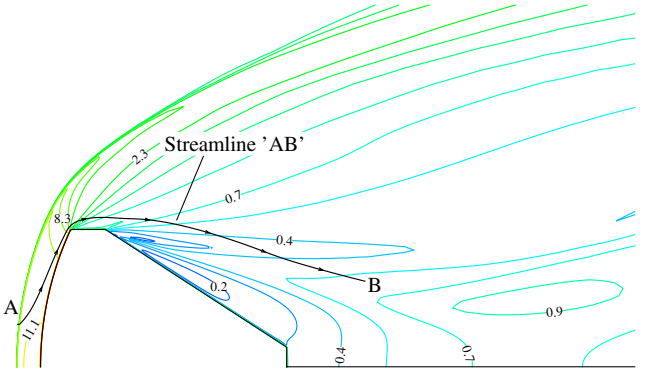


**Fig. 5 Distribution of the gas density, normalized by freestream density, in the flow around FIRE 2 reentry capsule.**

Figure 4a shows the computed surface heat transfer rate on the forebody as a function of the normalized arc length ($s/D$) measured from the nose of the vehicle. A value of $s/D = 0$ represents nose stagnation point and $s/D = 0.52$ is the first expansion corner. Heat transfer rate varies gradually on the forebody with a local maximum of 219 W/cm$^2$ at the nose. The stagnation point heating rate matches the theoretical estimate of Fay and Riddell [19]. At the expansion corner heating rate has a local peak followed by a sharp decrease, as the gas temperature drops due to flow expansion. The afterbody heat transfer rate is shown in Fig. 4b. The extent of the conical frustum and flat base are identified in the figure. The expansion corners are marked by local peaks in the heat transfer rate. In between the two expansion corners, the heating rate shows a monotonic increase from the separation point at the shoulder to the base corner. The base stagnation point heating rate is 22.48 W/cm$^2$, which is 10.3% of the corresponding nose stagnation point value. The computed afterbody heating rate compares well with the flight data (see Fig. 27 in [9]). The details of the comparison are omitted for the sake of brevity.

Figure 5 shows normalized density distribution in the flowfield. Density of the gas increases across the bow shock to 11 times the freestream density in the nose stagnation region. Rapid expansion at the shoulder reduces the density of the mixture to 0.2–0.4 $\rho_\infty$ on the afterbody. At the boundary layer (not visible on the scale of Fig. 5) gas temperature decreases to the cold wall value, which increases the mixture density to about $100\rho_\infty$ at the wall. The density of the gas in the afterbody near-wall region is about $2\rho_\infty$. Overall the density of the gas changes by three orders of magnitude in the computational domain, and it determines the degree of thermochemical activity in the different parts of the flowfield. The thermochemical state of the gas has an important influence on the surface heating rate as explained next.

The variation in the gas temperatures and composition at the shock wave are shown in Fig. 6. The data is plotted along the stagnation stream line such that the flow is in the positive $x$-direction and the nose stagnation point is at $x = 0$. The translational-rotational temperature peaks at about 8500 K immediately downstream of the shock wave, followed by rapid decrease due to transfer of translational energy into vibrational and chemical energies. The vibrational temperature shows a gradual rise to about 6200 K. As the chemical reactions progress, there is a drain of translational and vibrational energies. This results in decrease of both temperatures to a equilibrium value of 5700 K in the postshock region.

Oxygen molecules are mostly dissociated in the postshock region with an atomic oxygen mass fraction of 0.22. NO is formed behind the shock to a maximum level of 8%. It decreases to 2% in the postshock region. The exchange reactions result in an increase of $Y_N$ up to 0.05 and decrease of $Y_{N_2}$ to 0.71. The gas composition in the majority of the forebody inviscid region is close to the postshock values in Fig. 6b. The flow expansion at the shoulder results in a slight increase in $Y_{N_2}$ and $Y_O$ with a corresponding decrease in $Y_N$ and $Y_{NO}$. The gas composition in the afterbody inviscid expansion region is primarily composed of $N_2$ and O with mass fraction of 0.75 and 0.23, respectively. Minor changes in the mass fraction of $N_2$, N and NO are observed in the separation bubble due to chemical reactions in the hot vortex core.

The thermal state of the gas in the flowfield is explained with the aid of Fig. 7, which plots the translational-rotational and vibrational temperatures along a stream line (identified as streamline "AB" in

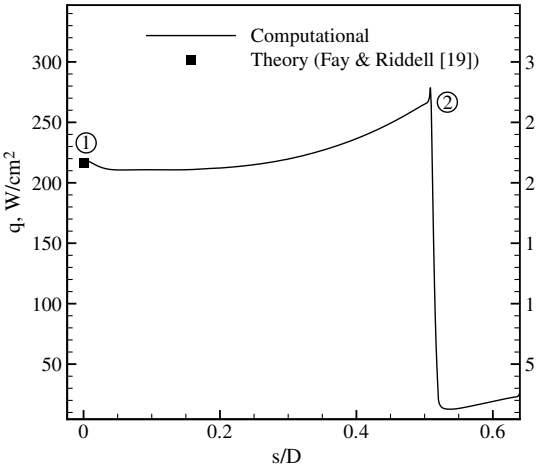


a)

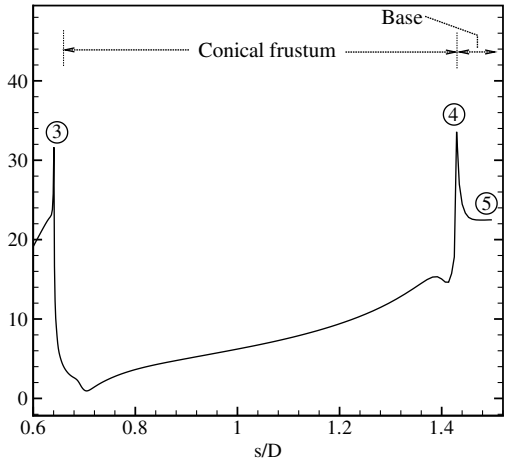


b)

**Fig. 4 Heat transfer rate computed on the a) forebody and b) afterbody of the FIRE 2 reentry capsule at Mach 16. Geometry points 1, 2, 3, 4, and 5 are identified in Fig. 1.**

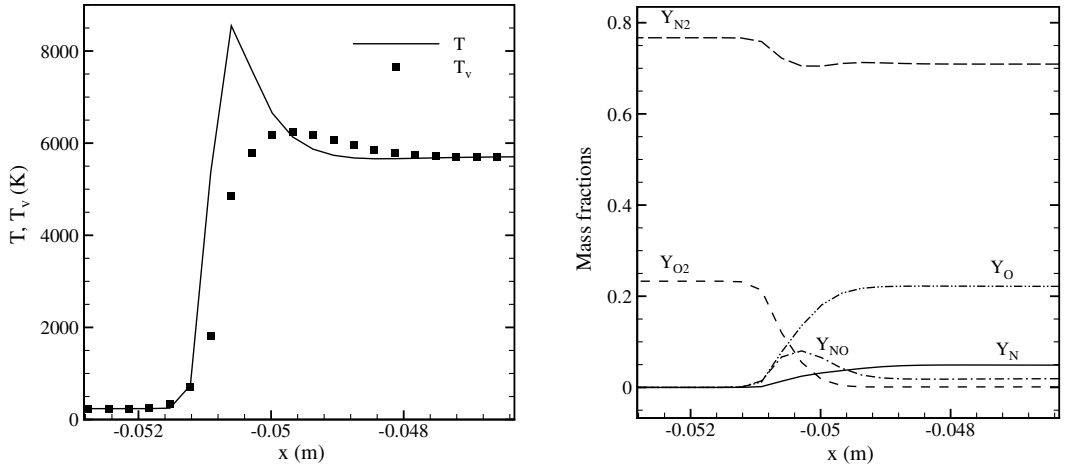


a) b)

**Fig. 6 Gas properties at the shock wave along the stagnation streamline: a) translational-rotational and vibrational temperatures and b) species mass fractions.**

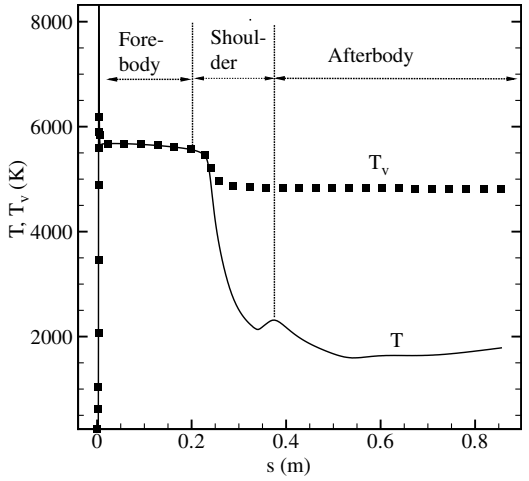


**Fig. 7 Translational-rotational and vibrational temperatures of the gas along a streamline (identified as streamline AB in Fig. 5) that passes through the bow shock wave, forebody and afterbody inviscid regions.**

Fig. 5) passing through the bow shock and the inviscid regions on the forebody, shoulder and afterbody. The two temperatures are identical in the postshock region on the forebody. A high fluid density in this region equilibrates both the translational and vibrational temperatures leading to a thermal equilibrium state. As the gas expands around the shoulder, a low density in the afterbody flowfield freezes the energy exchange between the translational and vibrational modes, resulting in a thermally frozen state on the afterbody. The vibrational temperature freezes at about 5000 K, whereas the translational-rotational temperature drops to values lower than 2000 K. The transition between the thermal equilibrium on forebody and frozen state on afterbody occurs through a thermal nonequilibrium state in the shoulder region. Chemical state of the gas follows a trend similar to that of the thermal state. The gas approaches a chemical equilibrium state in the nose stagnation region with a nonequilibrium state on the shoulder. The chemistry is in a frozen state in the afterbody region.

Figure 8a shows the variation of the two temperatures in the thermal boundary layer at the nose stagnation point. Local boundary-layer thickness is used to nondimensionalize the wall-normal distance, such that $l/\delta = 0$ represents the wall location and $l/\delta = 1$ corresponds to the thermal boundary-layer edge. Both the translational-rotational and vibrational temperatures of the gas decrease from 5700 K in the outer inviscid flow to 553.3 K at the isothermal wall. In the boundary-layer mass fraction of atomic

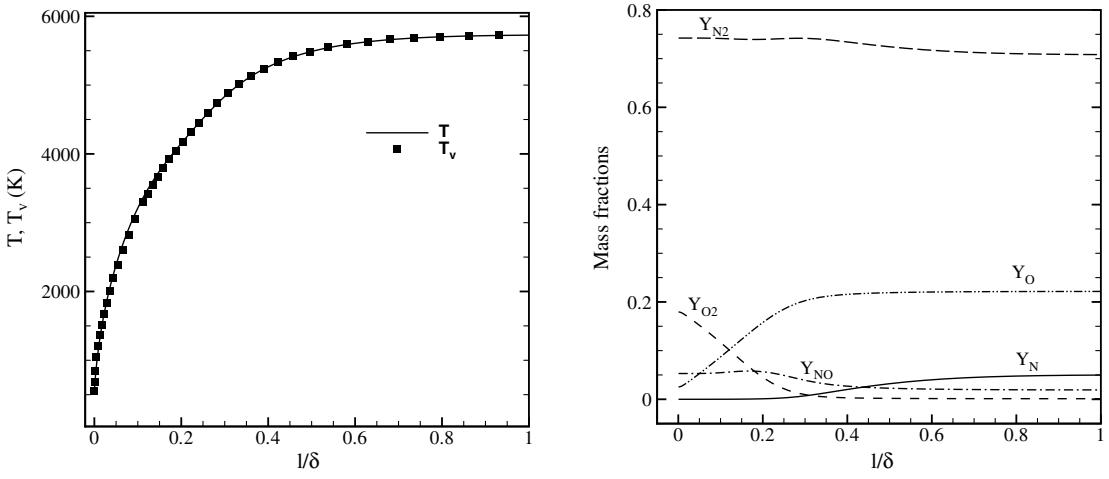


a) b)

**Fig. 8 Boundary layer profiles of a) translational-rotational and vibrational temperatures and b) species mass fractions at the nose stagnation point.**

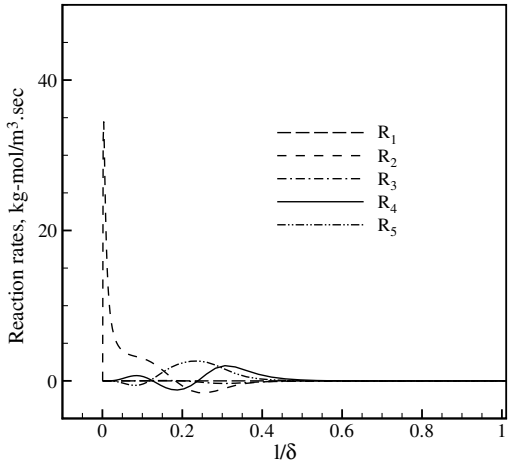


**Fig. 9 Rates of the different chemical reactions occurring in the thermal boundary layer at the nose stagnation point.**

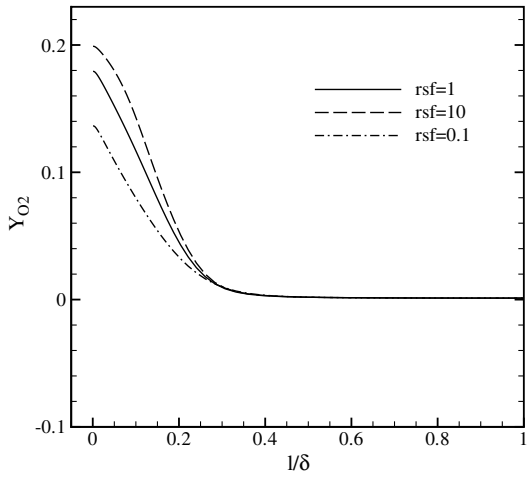


**Fig. 11 Effect of variation in reaction rates on $Y_{O_2}$ in the boundary layer at the nose stagnation point.**

species, i.e., O and N decrease, and a corresponding increase in mass fractions of $O_2$ and $N_2$ can be noticed in Fig. 8b. $Y_{NO}$ also increases from 0.02 at edge of boundary layer to 0.05 at wall.

Figure 9 depicts the rate of the different chemical reactions in the boundary layer. In the immediate vicinity of the wall, recombination of O is predominant and this leads to an increase in $Y_{O_2}$. The rate of the exchange reactions ($R_4$ and $R_5$) have nonnegligible values for $0.2 < l/\delta < 0.4$ and they increase the mass fractions of $N_2$ and NO with a corresponding decrease in $Y_N$. However these changes are smaller compared with the changes in oxygen mass fractions. In the outer portion of the boundary layer ($l/\delta > 0.5$), the reaction rates are approximately zero.

### A. Effect of Reaction Rate Variation on the Heating Rate

Figure 10 compares the forebody heat transfer rate obtained by varying the reaction rate constants with those of the baseline simulation (rsf = 1). Lowering the reaction rates in the boundary layer (rsf = 0.1) decreases the heating rate and enhancing the reaction rates (rsf = 10) results in an increase in the heat transfer rate. Also, the heating rate obtained by altering only the rate constant of oxygen recombination reaction are identical to that when all the five reactions rates are changed simultaneously. Therefore at the chosen freestream conditions, the surface heating rate is primarily sensitive to the rate of oxygen recombination, which is the dominant reaction in the near-wall region (see Fig. 9).

As noted earlier, the cold wall condition favors recombination reactions in the boundary layer. Increasing the reaction rates therefore enhances the formation of diatomic species. Figure 11 shows that in the boundary layer, the mass fraction of oxygen molecules increases for the higher reactivity case compared with the baseline simulation, and vice-versa. The recombination reactions are exothermic, and higher reactivity results in higher heat release. The gas temperature is therefore elevated in the rsf = 10 simulation as compared with baseline case. Opposite is true for lower reactivity simulation. This trend is depicted in Fig. 12a which shows the gas temperature at the first cell next to the wall.

The change in the gas composition due to recombination reactions leads to change in the mixture conductivity. For the current range of thermodynamic conditions, the relative magnitude of thermal conductivity among the species is

$$\kappa_N > \kappa_{O_2} > \kappa_{NO} > \kappa_{N_2} > \kappa_O \tag{5}$$

As molecular oxygen has higher thermal conductivity than its atomic counterpart, the rsf = 10 case has higher thermal conductivity of the gas mixture (see Fig. 12b). An elevated gas temperature and mixture conductivity in the higher reactivity case leads to the higher heating rate. The reverse is true for the lower reactivity simulation.

The heat flux to the wall can be written as

$$q = -\kappa \frac{\partial T}{\partial \eta} = -\kappa \frac{T_2 - T_w}{\Delta \eta} \tag{6}$$

where the mixture conductivity is a function of its composition and local thermodynamic condition. The wall-normal temperature gradient is discretized in terms of the gas temperature at the first cell next to the wall, the wall temperature, and the wall-normal distance, $\Delta\eta$. The change in heat flux due to varying reaction rates can therefore be expressed in terms of change in $\kappa$ and $T_2$. The quantities $T_w$ and $\Delta\eta$ remain fixed in all the three simulations:

$$\frac{\Delta q}{q} = \frac{\Delta \kappa}{\kappa} + \frac{\Delta T_2}{T_2 - T_w} \tag{7}$$

where higher-order terms are neglected. A quantitative analysis of the changes in heat transfer flux due to the varying reaction rates at different locations on the body is given next.

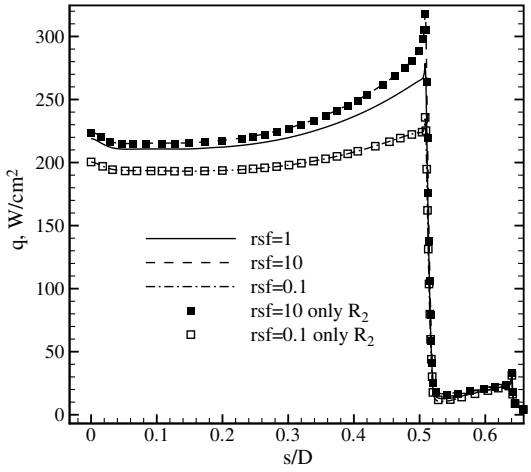


**Fig. 10 Effect of variation in reaction rates on the forebody surface heat flux.**

### B. Nose Stagnation Point

Table 2 shows a budget of Eq. (7) at the nose stagnation point for the higher and lower reactivity cases, where the changes are calculated with respect to the baseline solution. The positive values listed for rsf = 10 represent increase in the mixture conductivity and the gas temperature. The negative values, on the other hand, correspond to a reduction in the respective values when the reaction rate constants are decreased. The heating rate is enhanced by 2.4% for rsf = 10 and reduced by 8.5% for rsf = 0.1. Note that the stagnation point heating rate is more sensitive to lowering the

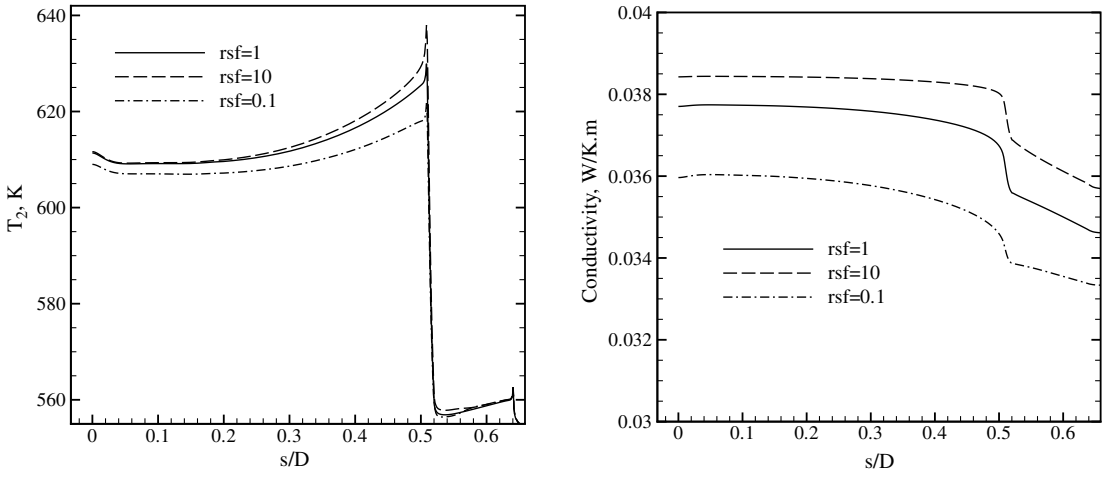


**Fig. 12 Changes in a) $T_2$ and b) mixture conductivity on forebody due to variation in reaction rates.**

reaction rates than to increasing the reactivity. A similar trend in heat transfer rate sensitivity is seen all along the forebody boundary layer (see Fig. 10). The reason for this trend in heating rate can be explained in terms of the chemical state of the gas (equilibrium, nonequilibrium or frozen) and the extent of the recombination reactions.

In the forebody shock layer, the gas is in chemical equilibrium, i.e., as $T \to T_w$, the gas composition approaches its equilibrium value given by the local thermodynamic conditions. Hence increasing the reaction rates does not alter the gas composition significantly. In the baseline simulations, majority of the atomic species recombine to form diatomic molecules. At the wall, the mass fraction of $O_2$ is close to its maximum achievable freestream value. Hence enhancing the recombination reactions further increases $O_2$ mass fraction by a small amount (0.02) (see Fig. 11), which has minimal effect on the heating rate. When reaction rates are decreased, recombination reactions are suppressed and it leads to an appreciable change in $O_2$ concentration in the boundary layer compared with the baseline solution. The heating rate is therefore altered significantly for lower reactivity case.

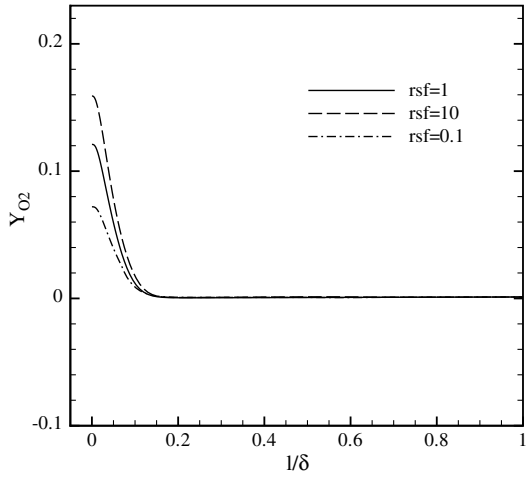


**Fig. 13 Change in $Y_{O_2}$ in the boundary layer at $s/D = 0.52$ (first expansion corner) due to variations in reaction rates.**

### C. Expansion Region

Figure 10 shows that the sensitivity of the surface heating rate to the reaction rate constants increases as we go from the stagnation point ($s/D = 0$) to the shoulder ($s/D = 0.51$). Similar trends can be observed in $T_2$ and $\kappa$ in Fig. 12. This is because of flow expansion along the forebody, which is characterized by a decrease in pressure, temperature and density with increasing distance from the stagnation point.

As the density decreases from the stagnation region to the shoulder, the reactions get slower and the chemical state of the gas changes from equilibrium to nonequilibrium. The gas composition does not approach equilibrium values corresponding to local thermodynamic condition at the cold wall temperature, and an appreciable fraction of the gas is in its atomic state. The extent of recombination is lower than that at the nose stagnation point and the mass fraction of $O_2$ molecules is not recovered to its freestream value. For example, at $s/D = 0.52$ located at the first expansion corner $Y_{O_2}$ reaches a value of 0.12 at the wall, as compared with a maximum possible value of 0.22 (see Fig. 13).

Increasing the reaction rate constants (rsf = 10) takes the gas closer to the chemical equilibrium state. It increases the extent of recombination (see Fig. 13) appreciably, which in turn results in an appreciable increase in the mixture conductivity and the gas temperature. Table 3 shows the contribution of $\Delta\kappa$ and $\Delta T_2$ to the overall heating rate enhancement at the expansion corner. Increased mixture conductivity (due to the additional $O_2$ recombination), and increased gas temperature (due to the exothermic reactions) result in a 16.8% enhancement in the surface heating rate. Decreasing the reaction rate constants (rsf = 0.1) has the opposite effect. It results in a significant decrease in $O_2$ mass fraction. The corresponding changes in $\Delta\kappa$ and $\Delta T_2$ are listed in Table 3 and they add up to a 15.2% decrease in the surface heating rate.

### D. Afterbody

The changes in surface heat flux along the afterbody frustum and base due to changes in the reaction rate constants are shown in

**Table 2 Contribution of $\Delta\kappa/\kappa$ and $\Delta T_2/(T_2 - T_w)$ to $\Delta q/q$ at the nose stagnation point**

| % change | rsf = 10 | rsf = 0.1 |
|---|---|---|
| $\Delta\kappa/\kappa$ | 1.91 | −4.61 |
| $\Delta T_2/(T_2 - T_w)$ | 0.48 | −4.08 |
| $\Delta q/q$ | 2.4 | −8.5 |

**Table 3 Contribution of $\Delta\kappa/\kappa$ and $\Delta T_2/(T_2 - T_w)$ to $\Delta q/q$ in the shoulder expansion corner ($s/D = 0.52$)**

| % change | rsf = 10 | rsf = 0.1 |
|---|---|---|
| $\Delta\kappa/\kappa$ | 3.92 | −5.55 |
| $\Delta T_2/(T_2 - T_w)$ | 12.38 | −10.22 |
| $\Delta q$ | 16.8 | −15.2 |

Fig. 14. Sensitivity of afterbody heating rate is much less than that observed on the forebody. Increasing the reaction rates results in only two appreciable changes in heat flux distribution. First, there is a rise in the base heating value as compared with the baseline simulation. Second, the location of the separation point (at $s/D \simeq 0.7$) changes, resulting in a corresponding variation in heating rate in this region. We study the flow solution at the base stagnation point ($s/D = 1.5$) in detail.

The lower sensitivity of the afterbody heat flux to the variation in reaction rates is due to a frozen chemical state of the gas in this region. This inhibits recombination reactions in the boundary layer as evident in Fig. 15a. Oxygen is mostly in its atomic form in the baseline (rsf = 1) simulation, with $Y_{O_2} \simeq 0.02$ at the wall. $Y_{O_2}$ increases to 0.05 for rsf = 10, and decreases below 0.01 for rsf = 0.1. Unlike the forebody and shoulder boundary layers, the changes in $Y_{O_2}$ observed in Fig. 15a are not entirely because of variation in reaction rate constants in the near-wall region. There is a noticeable difference between the $Y_{O_2}$ values computed at the edge of the boundary layer in the three simulations. The reason for this is explained next.

The gas that is trapped in the recirculation bubble originates from the forebody boundary layer. Changes in the gas composition in the forebody boundary layer caused by the variation in reaction rates is convected into the vortex core and free shear layer on the afterbody. This results in an appreciable variation in $Y_{O_2}$ at the boundary-layer edge between the three simulations. Changes in the mixture composition at the boundary-layer edge and increased reactivity in the boundary layer lead to an increase in the mixture conductivity by about 2.4% in the rsf = 10 simulation. The conductivity decreases by about 1.5% in the lower reactivity case (see Table 4).

**Table 4 Contribution of $\Delta\kappa/\kappa$ and $\Delta T_2/(T_2 - T_w)$ to $\Delta q/q$ at base stagnation point ($s/D = 1.5$)**

| % change | rsf = 10 | rsf = 0.1 |
|---|---|---|
| $\Delta\kappa/\kappa$ | 2.38 | −1.46 |
| $\Delta T_2/(T_2 - T_w)$ | 2.32 | 1.77 |
| $\Delta q$ | 4.76 | 0.27 |

Similar to the mixture conductivity, the gas temperature adjacent to the wall is also determined by a combination of the boundary-layer edge effect and the changes caused by altering the reaction rates in the near-wall region. Figure 15b shows that the boundary-layer edge temperature is lower for rsf = 10 compared with the baseline simulation and it counteracts the increase in $T_2$ due to enhanced exothermic reactions in the boundary layer. The opposite is true for rsf = 0.1 solution. The net effect is an increase in $T_2$ by 2.3% in the higher reactivity case and an increase of 1.8% in the lower reactivity simulation (see Table 4). For rsf = 10 case, changes in gas temperature add to the changes in the mixture conductivity leading to a 4.8% increase in the base heating rate. On the other hand, changes in $\kappa$ and $T_2$ due to reduced reaction rates cancel each other to yield a negligible effect on the base heating rate for rsf = 0.1.

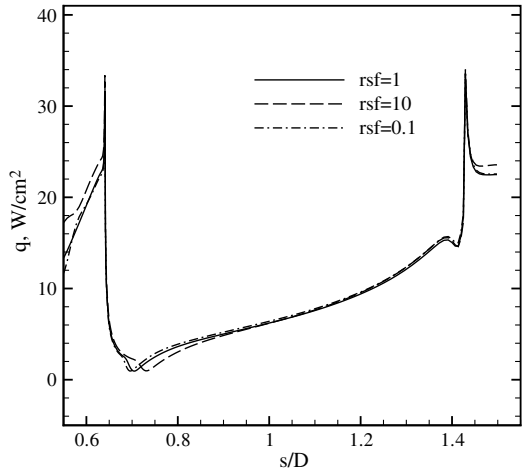


**Fig. 14 Effect of variation in reaction rates on the afterbody heating rate.**

### E. Increase of Reaction Rates in the Entire Computational Domain

Figure 16 compares the flowfield solutions obtained from the baseline simulation (top half) and a higher reactivity simulation in which the rate constants are increased (rsf = 10) uniformly over the entire computational domain. The shape of the bow shock wave, the shock standoff distance and the temperature of the gas in the inviscid shock layer are essentially same in the two solutions. However the afterbody flowfield shows some marked changes. In the higher reactivity simulation, the separation point shifts downstream compared with that of the baseline case, resulting in a significant reduction in the separation bubble size. A lip shock originating at the separation point can be clearly seen in the higher reactivity case, and the shear layer angle is lower by 2.32° as compared with the baseline simulation.

The variation of gas temperature and $Y_{NO}$ along the stagnation stream line is shown in Fig. 17. Increased reactivity (rsf = 10) at the shock wave enhances the dissociation of $N_2$ and $O_2$, leading to a higher level of NO formation. As the dissociation is an endothermic process, higher dissociation at the shock wave leads to a lower temperature (by about 1000 K) than the baseline solution.

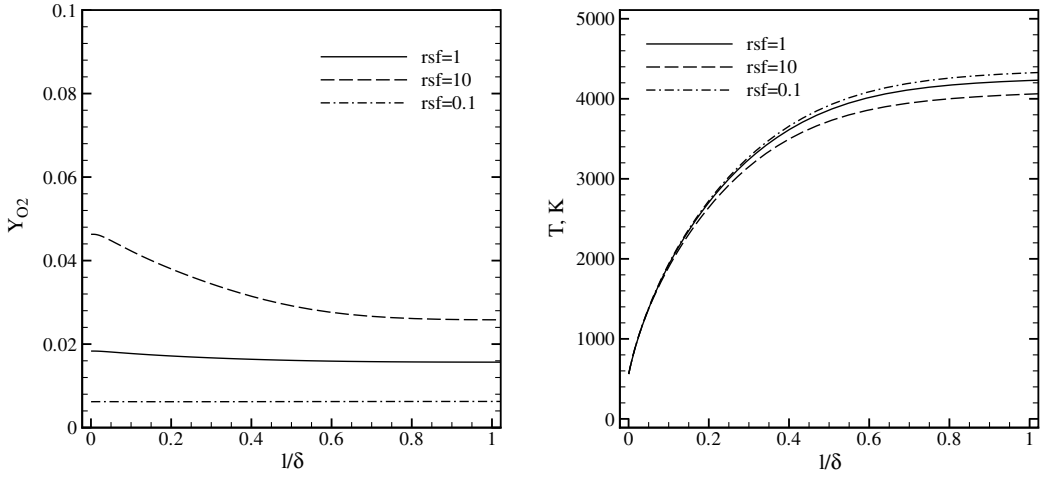


a) b)

**Fig. 15 Profiles of a) $Y_{O_2}$ and b) temperature in the thermal boundary layer at the base stagnation point.**

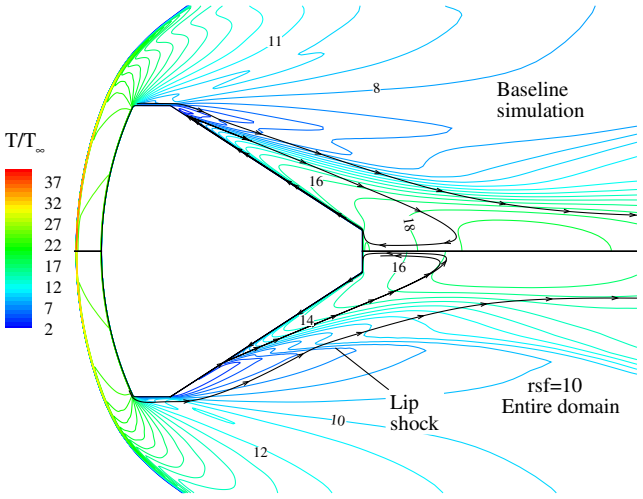


**Fig. 16 Comparison of nondimensional temperature distribution and separation bubble obtained from the baseline (top half) and higher reactivity (bottom half) simulations. Streamlines are drawn to demarcate the separation point and recirculation bubble size.**

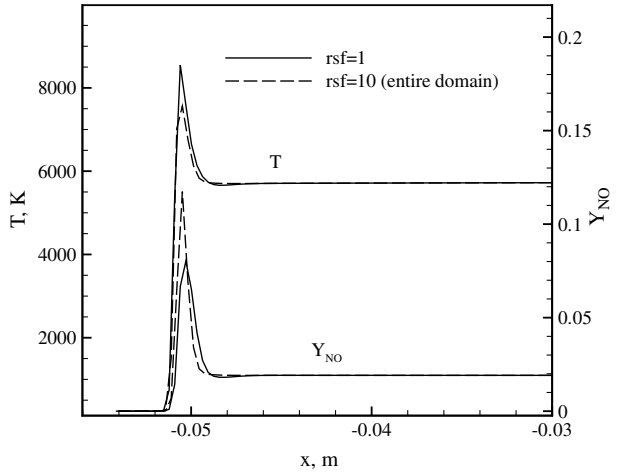


**Fig. 17 Effect of increasing the reaction rates in the entire domain on gas temperature and $Y_{NO}$ along the stagnation streamline.**

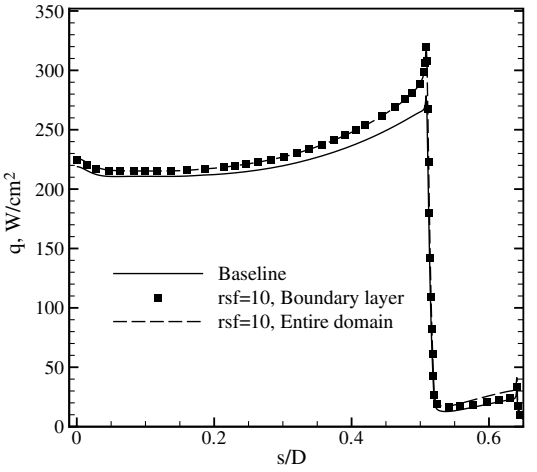


**Fig. 18 Effect of increasing the reaction rates in the entire domain on forebody heating rate.**

Downstream of the shock wave, the two solutions are identical in terms of $T$ and $Y_{NO}$. This corresponds to the thermochemical equilibrium region, where $T = T_v$ and all the species concentrations attain their equilibrium values. This gives identical solution at the boundary-layer edge in the baseline and higher reactivity simulations. Further changes in the thermal boundary layer in the higher reactivity case match those obtained (see Fig. 11) when the reaction rates are enhanced only in the near-wall region. This is reflected in the overlapping heat transfer predictions obtained from the two rsf $= 10$ simulations in Fig. 18.

The gas approaches thermochemical equilibrium in the entire region between the bow shock and the spherical forebody. As a result, the changes in $T$ and $Y_{NO}$ induced by higher reactivity at the shock (see Fig. 17) have a negligible effect on the shape and location of the bow shock. Also, the changes at the shock wave have no effect on the surface heating augmentation on the entire forebody, up to the first expansion corner (see Fig. 18).

Increasing the reaction rates outside the boundary layer has a much larger effect on the surface heat flux at the shoulder. Flow expansion in this region and the associated temperature drop causes recombination and exchange reactions. The gas is in a state of thermochemical nonequilibrium, so that increasing the chemical rate constants results in a higher degree of these reactions. The gas chemistry in this zone is exothermic, and therefore a higher reactivity results in a hotter gas in the outer inviscid flow than in the baseline simulation. Figure 19a shows this effect in terms of the temperature

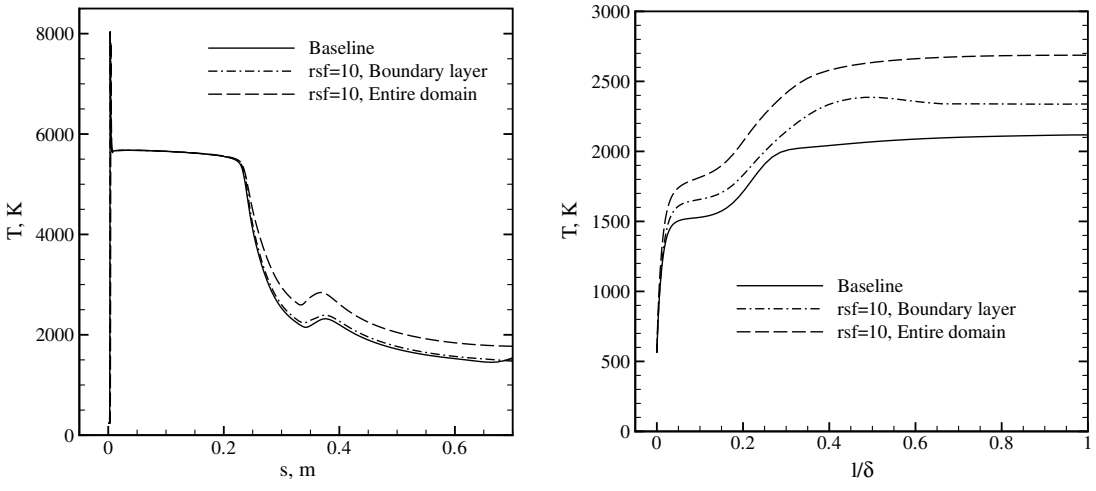


**a)** **b)**

**Fig. 19 Effect of increasing the reaction rates on gas temperature: a) along the streamline AB, shown in Fig. 5, and b) across the boundary layer at the second expansion corner, $s/D = 0.64$.**

**Table 5 Contribution of $\Delta\kappa/\kappa$ and $\Delta T_2/(T_2 - T_w)$ to $\Delta q/q$ at the second expansion corner ($s/D = 0.64$) in the two higher reactivity simulations**

| % change | Boundary layer | Entire domain |
|---|---|---|
| $\Delta\kappa/\kappa$ | 3.22 | 3.02 |
| $\Delta T_2/(T_2 - T_w)$ | 2.37 | 27.37 |
| $\Delta q$ | 5.70 | 32.01 |

**Table 6 Contribution of $\Delta\kappa/\kappa$ and $\Delta T_2/(T_2 - T_w)$ to $\Delta q/q$ at the at base stagnation point ($s/D = 1.5$) in the two higher reactivity simulations**

| % change | Boundary layer | Entire domain |
|---|---|---|
| $\Delta\kappa/\kappa$ | 2.38 | 2.51 |
| $\Delta T_2/(T_2 - T_w)$ | 2.32 | 16.89 |
| $\Delta q$ | 4.76 | 18.23 |

distribution along the streamline AB that spans the inviscid region on the forebody, shoulder and afterbody.

An elevated gas temperature in the rsf = 10 simulation increases the surface heating rate on the shoulder ($0.54 < s/D < 0.64$), as can be observed in Fig. 20a. The effect is localized in the vicinity of the first expansion corner, when the reaction rates are altered only in the near-wall region. The gas chemistry is frozen in the later part of expansion, leading to heating rates comparable to the baseline predictions. By comparison, when the reaction rates are altered in the entire domain, its effect is carried further by the inviscid flow outside the boundary layer. The resulting increase in gas temperature at the boundary-layer edge (see Fig. 19b) has a major effect. The heating rate in this case is enhanced over the entire shoulder region, up to the second expansion corner. Table 5 shows the contribution of $\Delta\kappa$ and $\Delta T_2$ to the heating rate increment at $s/D = 0.64$ obtained from the two higher reactivity simulations. The change in the mixture conductivity is similar in the two cases. The dominant effect is the increase of $\Delta T_2$ when rsf = 10 in the entire domain and it raises the surface heat flux by 32%.

The effect of increased reactivity on surface pressure (see Fig. 20b) is similar to that observed for the heat flux. Compared with the baseline values, the pressure level on the shoulder is elevated when the reaction rates are enhanced by a factor of 10.

On the conical frustum, heating rates predicted by the three simulations follow the same trend (see Fig. 20a). There is a rapid drop in heat transfer at the expansion corner, followed by a local minimum at the separation point. The heating rate increases along the separation bubble, with a relatively high value at the base stagnation point. Enhanced reactivity in the entire domain shifts the separation point downstream (also see Fig. 16). There is a slight increase in the heat flux on the later part of the conical frustum and a relatively larger increase in the base heating rate compared with the baseline simulation. Similar trends, but smaller in magnitude, are also observed when the reaction rates are altered only in the near-wall region.

The pressure data shown in Fig. 20b shows a similar pattern. The pressure rise at the separation point is shifted downstream for higher reactivity cases. As expected, altering the rate constants only in the near-wall region has negligible effect on the pressure distribution. On the other hand, enhanced reactivity in the entire domain changes the size and shape of the separation bubble, resulting in a higher pressure on the afterbody frustum and base.

Note that enhancing the reaction rate constants in the entire domain increases the base heating rate by about 18.2% of the baseline value. Table 6 lists the contributions of increased mixture conductivity and gas temperature to the rise in surface heating. The change in mixture conductivity and therefore the extent of recombination in this case are similar in magnitude to that obtained when the chemical rate constants are altered only in the boundary layer. However, the gas temperature in the immediate vicinity of the wall is significantly higher for the case of enhanced reactivity in the entire domain. As discussed earlier (Sec. III.D), the gas temperature and the mixture composition at the base stagnation point are determined by a combined effect of their boundary-layer edge values and by the extent of exothermic recombination reactions in the boundary layer. The effect of enhanced reactivity in the outer flow on boundary-layer edge values is the dominant factor in raising the heating rate. The chemical reactions in the near-wall region has a minor effect on the surface heat flux. This is due to the low density and consequently a frozen thermochemical state of the gas in this region.

### F. Decrease of Reaction Rates in the Entire Computational Domain

Figure 21 compares of nondimensional temperature contours and separation bubble streamlines obtained from the baseline case (top half) and the lower reactivity simulation (bottom half) in which rate constants are decreased (rsf = 0.1) uniformly in the entire computational domain. In the lower reactivity case, the gas temperature at the bow shock wave is higher, and the shock standoff distance marginally increases compared with the baseline simulation. Location of the separation point and the shear layer angle are approximately same in both solutions. The separation bubble is, however, slightly larger in the lower reactivity case than the baseline simulation.

The variation of gas temperature and $Y_{NO}$ along the stagnation stream line (Fig. 22) shows that the shock wave moves slightly upstream when the reaction rates are reduced. A decrease in reaction

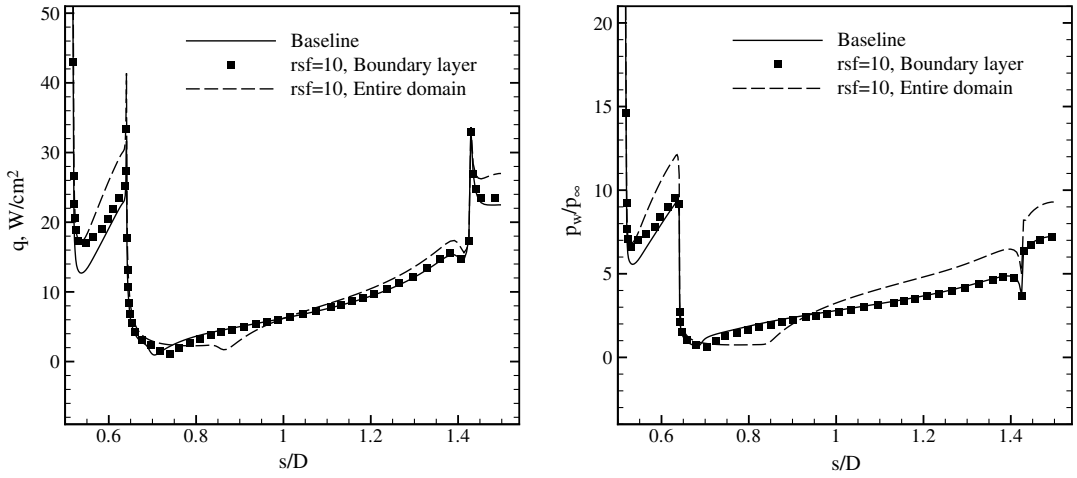


a) b)

**Fig. 20 Effect of increasing the reaction rates in the entire domain on afterbody surface properties: a) heat transfer and b) normalized pressure.**

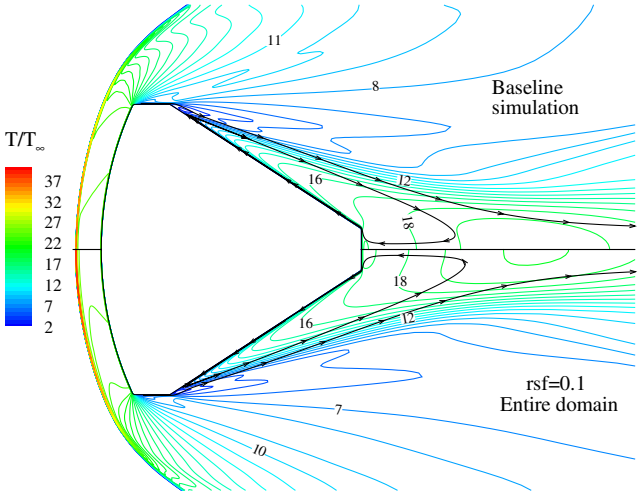


**Fig. 21 Comparison of nondimensional temperature distribution and separation bubble between the baseline (top half) and lower reactivity (bottom half) simulations.**

rates suppresses the dissociation of $N_2$ and $O_2$. This leads to lower level of NO and a higher peak temperature at the shock. The trend is exactly opposite to that observed in the higher reactivity case (cf. Figure 17). A lower reactivity also results in a slower approach to the thermochemical equilibrium state downstream of the shock. As expected, the gas properties in the equilibrium region are identical in the two solutions. This results in identical values at the boundary-layer edge. Further changes in the thermal boundary layer in the lower reactivity case match those obtained (in Fig. 11) when the reaction rates are suppressed only in the near-wall region. The heat transfer rates predicted by the lower reactivity (entire domain) simulation is same as the rsf = 0.1 values presented in Fig. 10 over majority of the forebody surface and hence not repeated here.

A lower reactivity suppresses the recombination and exchange reactions in the shoulder expansion region. This results in a lower mass fraction of the molecular species and a lower gas temperature. Both lead to a reduction in surface heat flux (see Fig. 23a) on the shoulder, as explained in Sec. III.C. Once again, the effect is localized in the vicinity of the first expansion corner when the reaction rate constants are decreased only in the boundary-layer region. For the case with reduced reactivity in the entire domain, the surface heating rate is reduced over the entire shoulder region ($0.52 < s/D < 0.64$). A similar reduction in the surface pressure on the shoulder can be seen in Fig. 23b.

The afterbody surface data presented in Fig. 23 shows a marginal reduction in heating rate when the rate constants are decreased in the entire flowfield. The base heat flux is lower than the baseline value by 6.5%. The pressure predictions show a relatively larger deviation from the baseline values, with a 16% reduction at the base stagnation point when the rate constants are lowered in the entire domain. The surface pressure is found to be more sensitive than the heat transfer rate to variation in separation bubble size, reported in Fig. 21.

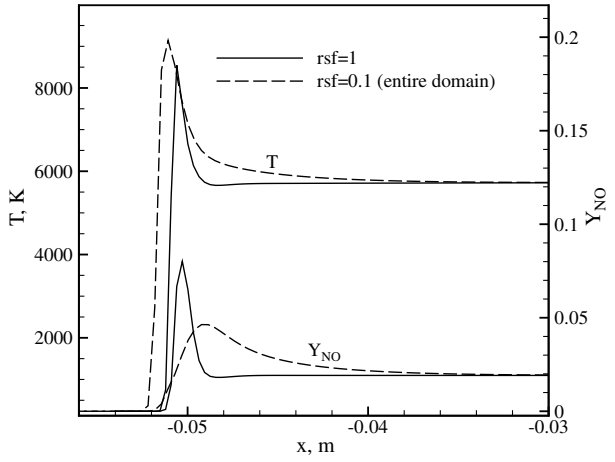


**Fig. 22 Effect of decreasing the reaction rates in the entire domain on gas temperature and $Y_{NO}$ along the stagnation streamline.**

## IV. Discussion

In a reentry flowfield, the interaction of thermochemistry with the fluid dynamics is a complex phenomena. Changes in the thermodynamic properties of the gas, induced by shock waves, expansion and flow separation initiate the thermochemical relaxation processes. Variations in thermochemical rates in turn affect the flow solution and therefore the surface heat flux predictions. From the preceding analysis, we can summarize that the following factors affect the heat transfer rate sensitivity to the variation in reaction rates: 1) dominant chemical reaction(s) in the gas mixture; 2) chemical state of the gas: equilibrium, nonequilibrium or frozen; and 3) extent of recombination in the boundary layer.

At the current freestream conditions, typical of a low altitude trajectory point, recombination of oxygen atoms in the vicinity of the cold wall is the main chemical reaction occurring in the boundary layer. Increasing the reaction rate constant favors recombination, which is exothermic, and therefore tends to elevate the gas temperature. Higher reactivity also alters the gas composition so as to increase the mixture conductivity. Both lead to enhanced heat transfer rate to the vehicle surface. Reduction in the reaction rate has

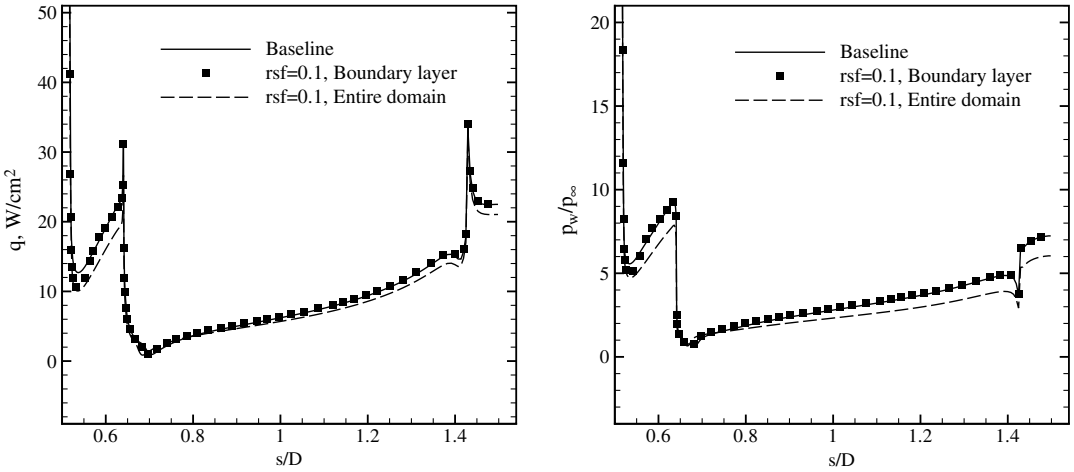


**a)** **b)**

**Fig. 23 Effect of decreasing the reaction rates in the entire domain on afterbody surface properties: a) heat flux and b) normalized pressure.**

**Table 7 Summary of the main factors that affect the sensitivity of heating rate to variation in reaction rate constants. Positive and negative values indicate increase and decrease in heat transfer rate with reference to the baseline simulation**

| | Forebody | Shoulder | Afterbody |
|---|---|---|---|
| Chemical state of the gas | Equilibrium | Nonequilibrium | Frozen |
| Extent of recombination | High | Medium | Low |
| Sensitivity to higher reactivity | 2% | 32% | 18% |
| Sensitivity to lower reactivity | −9% | −16% | −6% |

the opposite effect. Exchange reactions are also active in the inviscid expansion region around the shoulder. These reactions are in the exothermic direction and they have same effect on the heat flux as the exothermic recombination reactions in the boundary layer. Table 7 summarizes the overall trends in heating rate when the reaction rates are varied.

Table 7 also lists the chemical state of the gas and the extent of recombination at the forebody, shoulder and afterbody locations. On the forebody the gas composition approaches equilibrium state, and oxygen recombination is mostly complete. Increasing reaction rate further has a small effect on the gas properties and the surface heat flux. On the other hand, decreasing the rate constants lowers the heating rate significantly. Opposite is true on the afterbody, where a frozen chemical state results in oxygen predominantly being in the atomic form. Decreasing reaction rates has a small effect here, whereas there is significant increase in heating rate when the reaction rates are enhanced.

The forebody and afterbody analyses highlight the two ends of the chemical spectrum, i.e., equilibrium and frozen. The nonequilibrium flow in the shoulder region lies in between these two limiting cases. Here, both increasing and decreasing the reaction rates have significant effect on the heat transfer rate, and the sensitivity of the shoulder heating rate is found to be highest along the entire vehicle surface.

The range of conditions prevailing in the current FIRE 2 flowfield results in chemical equilibrium, nonequilibrium and frozen states on different parts of the vehicle. This allows us to study the heating rate sensitivity in all the three regimes in a single test case. It is found that increasing the chemical reaction rates has minimal effect on the surface heating when the flow is close to chemical equilibrium. This is the case at the nose stagnation point of the current test case. Nose stagnation point heating rate is often used for thermal protection system (TPS) sizing. Therefore the fact that the nose stagnation point heating may not increase further due to uncertainties in chemical reaction rates may be beneficial to the TPS sizing.

At higher altitudes, a lower freestream density can result in a chemical nonequilibrium state in the nose stagnation region. In such a case, the stagnation point heating rate can exhibit higher sensitivity to the chemical rate constants, similar to what is observed at the shoulder expansion region of the current flowfield. Also, additional chemical reactions at higher enthalpy conditions, uncertainties in mixture conductivity calculations, and variation in surface catalytic properties can induce other physical effects, which can influence the sensitivity of heating rate. A careful analysis of these factors requires further investigation.

## V. Conclusions

Sensitivity of the aeroheating predictions over FIRE 2 reentry capsule at 35 km altitude is studied by changing the chemical reaction rates from their baseline values reported in the literature. Reaction rate constants (both forward and backward) are increased by a factor of 10 and then decreased by a factor of 10, while keeping the equilibrium constant same. At the current freestream conditions, typical of a low altitude reentry trajectory point, the bow shock wave shape and position are not sensitive to the variation in reaction rates. Surface heat transfer rate is mainly sensitive to the variation in oxygen atom recombination rate in the boundary layer and to the variation in the exchange reaction rates in the inviscid expansion region around the shoulder. Increasing the reaction rate enhances the surface heating rate, and vice versa. Nose stagnation point heat flux is found to be relatively insensitive to an increase in the chemical reactivity. This is due to the fact that recombination of oxygen atoms is mostly complete in this region. A higher sensitivity is observed at the shoulder region, where the gas is in a chemical nonequilibrium state and oxygen atoms are partially recombined. The afterbody flowfield is in a chemically frozen state, and there is little chemical activity in the near-wall region. The changes in the afterbody aerothermal predictions is mainly due to the variation in the separation bubble size when the rate constants are altered. In summary, the current work brings out the complex interplay between chemical kinetics and fluid dynamics in a reentry flowfield, and its effect on the heat flux at the vehicle surface.

## Acknowledgment

The authors thank Indian Space Research Organization for supporting this research under the RESPOND program.

## References

[1] Bertin, J. J., *Hypersonic Aerothermodynamics*, AIAA Education Series, AIAA, Washington, D.C., 1994, pp. 143–149.

[2] Prabhu, D. K., Loomis, M. P., Venkatapathy, E., Davies, C. B., and Henline, W. D., "X-33 Aerothermal Environment Simulations and Aerothermodynamic Design," AIAA Paper 1998-0868, 1998.

[3] Candler, G. V., and Olejniczak, J., "Nitrogen Dissociation Rates in Complex Hypersonic Flows," AIAA Paper 1997-2500, 1997.

[4] Gnoffo, P. A., Weilmuenster, K. J., Hamilton II, H. H., Olynick, D. R., and Venkatapathy, E., "Computational Aerothermodynamic Design Issues for Hypersonic Vehicles," *Journal of Spacecraft and Rockets*, Vol. 36, No. 1, Jan.–Feb. 1999, pp. 21–43. doi:10.2514/2.3430

[5] Bose, D., and Wright, M. J., "Uncertainty Analysis of Laminar Aeroheating Predictions for Mars Entries," AIAA Paper 2005-4682, 2005.

[6] Palmer, G. E., "Uncertainty Analysis of CEV LEO and Lunar Return Entries," AIAA Paper 2007-4253, 2007.

[7] Tchuen, G., and Zeitoun, D., "Effects of Chemistry in Nonequilibrium Hypersonic Flow Around Blunt Bodies," *Journal of Thermophysics and Heat Transfer*, Vol. 23, No. 3, July–Sept. 2009, pp. 433–442. doi:10.2514/1.42665

[8] Slocumb, T. H., "Project FIRE Flight 2 Afterbody Temperatures and Pressures at 11.35 Kilometers per Second," NASA TM X-1319, 1966.

[9] Reddy, D. S. K., and Sinha, K., "Hypersonic Turbulent Flow Simulation of FIRE 2 Reentry Vehicle Afterbody," *Journal of Spacecraft and Rockets*, Vol. 46, No. 4, July–Aug. 2009, pp. 745–757. doi:10.2514/1.41380

[10] Park, C., *Non-Equilibrium Hypersonic Aerothermodynamics*, Wiley-Interscience, New York, 1990, pp. 35, 255–268, 326.

[11] Blottner, F. G., Johnson, M., and Ellis, M., "Chemically Reacting Viscous Flow Program for Multicomponent Gas Mixtures," Sandia Labs. Rept. No. SC-RR-70-754, Albuquerque, NM, 1971.

[12] Vincenti, W. G., and Kruger, C. H., *Introduction to Physical Gas Dynamics*, Krieger, Malabar, FL, 1986, p. 407.

[13] Wilke, C. R., "A Viscosity Equation for Gas Mixtures," *Journal of Chemical Physics*, Vol. 18, No. 4, 1950, pp. 517–519. doi:10.1063/1.1747673

[14] MacCormack, R. W., and Candler, G. V., "The Solution of the Navier–Stokes Equations Using Gauss–Siedel Line Relaxation," *Computers and Fluids*, Vol. 17, No. 1, 1989, pp. 135–150. doi:10.1016/0045-7930(89)90012-1

[15] Sinha, K., and Candler, G. V., "Convergence Improvement of Two-Equation Turbulence Model Calculations," AIAA Paper 98-2649, 1998.

[16] Wright, M. J., Candler, G. V., and Bose, D., "Data-Parallel Line Relaxation Method for the Navier–Stokes Equations," *AIAA Journal*, Vol. 36, No. 9, 1998, pp. 1603–1609. doi:10.2514/2.586

[17] Spalart, P. R., and Allmaras, S. R., "A One-Equation Turbulence Model for Aerodynamic Flows," AIAA Paper 92-0439, 1992.

[18] Nompelis, I., and Candler, G. V., "Investigation of Hypersonic Double-Cone Flow Experiments at High Enthalpy in the LENS Facility," AIAA Paper 2007-203, 2007.

[19] Fay, J. A., and Riddell, F. R., "Theory of Stagnation Point Heat Transfer in Dissociated Air," *Journal of the Aeronautical Sciences*, Vol. 25, No. 2, Feb. 1958, pp. 73–85.